Supplementary Information for

Photodissociation of CF_3CHO provides a new source of CHF_3 (HFC-23) in the atmosphere: implications for new refrigerants

Jyoti S. Campbell,[1] Scott H. Kable,[1] Christopher S. Hansen[1*]

[1]School of Chemistry, University of New South Wales, Sydney NSW 2052, Australia

[*]Correspondence and requests for materials to: christopher.hansen@unsw.edu.au

Supplementary Methods

CF_3CHO Synthesis

Trifluoroacetaldehyde (CF_3CHO) was prepared by dehydrating the monohydrate (Merck, 75% in water) using a literature method (34). The CF_3CHO was trapped in liquid nitrogen and the atmosphere removed before it was allowed to evaporate into a stainless-steel (316 grade) gas cylinder and diluted to 2% (v/v) in helium (N5.0). The purity was verified by FT-IR revealing no unreacted precursor, carbon dioxide or water. FT-IR spectra were collected throughout and beyond the experimental acquisition period revealing no degradation of the sample on a timescale of weeks. See Fig. S1 for a representative FT-IR spectrum of CF_3CHO sample in helium.

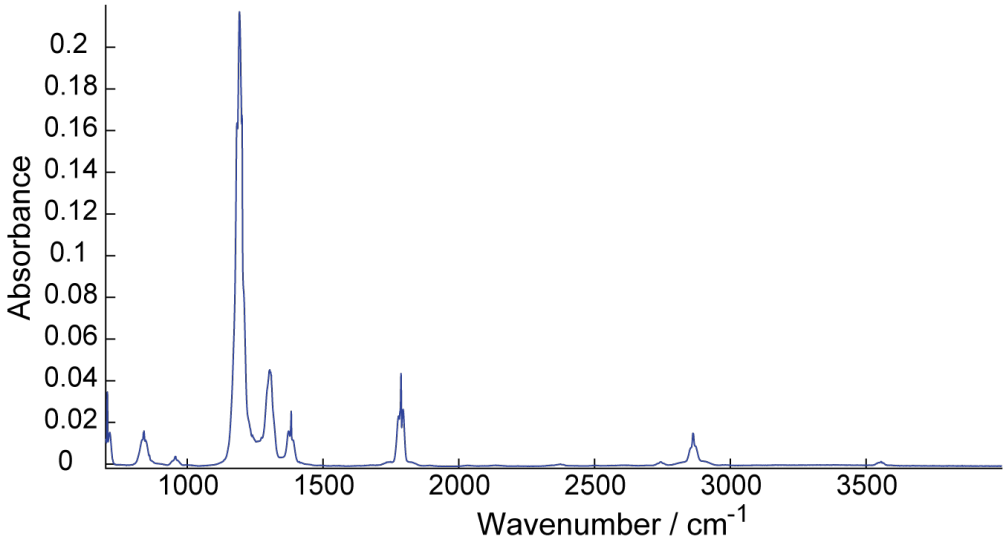

Figure S1: Representative FT-IR spectrum of an unirradiated CF_3CHO sample.

Photon Sources

The 308 nm photolysis laser used was the frequency-doubled output of a dye laser (Lambda-Physik LPD3000) operating with a mixture of Rhodamine 610 and Rhodamine 640 and pumped by the second harmonic (532 nm) of a nanosecond Nd:YAG laser (Quantel Brilliant B). Approximately 1.5 mJ of energy per pulse was coupled into the interaction region using an $f = 500$ mm quartz lens.

The 230 nm probe laser used for resonance-enhanced multiphoton ionisation of CO was the frequency-doubled output of a dye laser (Sirah Cobra-Stretch, 2×1800 g/mm grating model) using Coumarin 460 dye and pumped by the third harmonic (355 nm) of a nanosecond Nd:YAG laser (Spectra-Physics Quanta-Ray Pro-230), attenuated with a long Q-switch delay, to ultimately produce $\sim$100 μJ of UV light that was focused into the interaction region using an $f = 500$ mm quartz lens.

The 115 nm probe laser used to ionise the radical fragments employed the same laser system used to probe CO at $\sim$230 nm, this time pumped with the Nd:YAG second harmonic (532 nm) and using Pyridine 1 (LDS 698) laser dye. The 345 nm output with a pulse energy of 13 mJ was frequency tripled to 115 nm by focusing it, using an $f = 250$ mm quartz lens, into a 350 mm long stainless-steel gas cell mounted directly onto the imaging spectrometer and filled to approximately 1.3 bar with a $\sim$1:5 ratio of krypton (N4.8) in argon (N5.0). The VUV light was coupled to the molecular beam using a LiF lens ($f = 100$ mm at 121.6 nm), which also seals the gas cell from the vacuum chamber. The design of this cell is similar to one described in detail previously [31].

Molecular beam

The molecular beam was generated using a 0.5 mm orifice pulsed poppet valve (General Valve Series 9 driven by an Iota One valve driver) and passed through a skimmer with a 1 mm orifice mounted on a bulkhead at a distance of approximately 50 mm. Gas mixes containing 2% (v/v) target molecule, unless otherwise specified, in a carrier gas of helium (N5.0) were introduced to the valve at a stagnation pressure of 1.8 bar. The CF_3CHO mix was prepared as described above. The CH_3CHO mix was prepared daily by degassing a liquid sample of CH_3CHO (Merck, $\geq$ 99.5%) through at least three freeze-pump-thaw cycles and until no gas evolution was evident on thawing, then collecting the vapour off the degassed sample.

Supplementary Discussion

Section S1 – Radical Channel R1

To study the radical channel, we employed velocity-mapped ion imaging (VMI) coupled with vacuum ultraviolet (VUV) ionisation to detect HCO and CF_3/CH_3 photoproducts in all quantum states simultaneously. Fig. S2A shows the total kinetic energy release distributions inferred from both CF_3 and CHO fragments following photolysis of CF_3CHO at 308 nm. Firstly, the distributions are superimposable, which demonstrates that they are momentum matched and arise from the same mechanism and precursor. Secondly, the distributions have an overall Gaussian shape, peaking away from zero speed. This is characteristic of a reaction occurring over a barrier, such as the barrier calculated on the triplet surface of CF_3CHO. The distributions strongly resemble those recorded for CH_3CHO in this study and shown in Fig. S2B. The final observation from these distributions concerns the energy indicated by the vertical line in Fig. S2A. This line is located at the theoretical maximum total kinetic energy release, according to our calculations above. The experimental distribution converges on this line, which provides experimental benchmarking of the calculated bond dissociation energy.

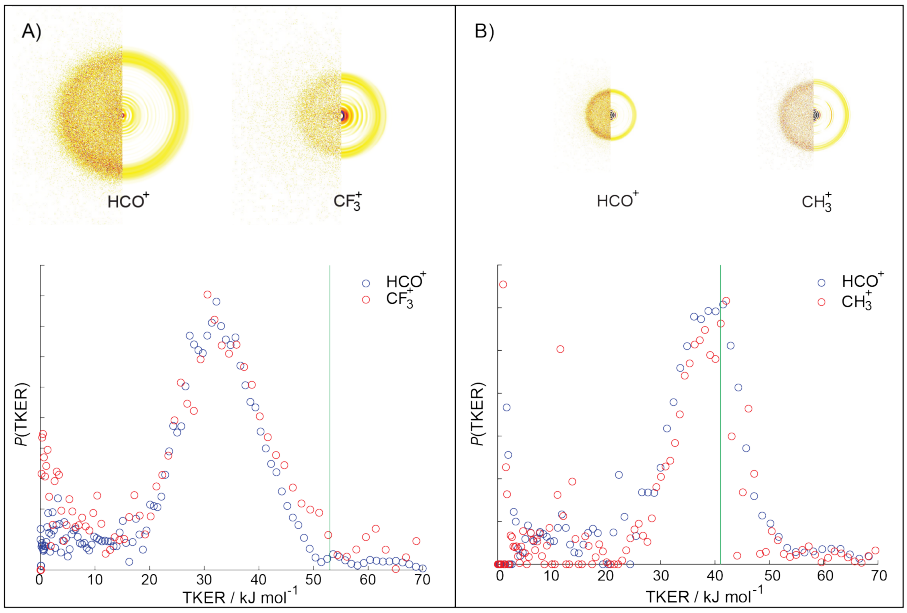

Figure S2: Ion images and total kinetic energy release distributions for the radical products of reaction pathway R1 following 308 nm photolysis of (A) CF_3CHO and (B) CH_3CHO as described in the text.

This channel also allowed us to perform several checks to verify that the molecular beam conditions were producing negligible clusters. It is known from earlier work that CH_3CHO can form clusters under certain molecular beam conditions leading to CH_3 and CHO photolysis products exhibiting near-zero kinetic energy [17]. The dominant feature in each of the ion images in Fig. S2 is an anisotropic anulus with negligible slow ion signal. There is, however, some intensity corresponding to zero velocity that is most evident in the CF_3^+ ion image in Fig. S2A. We record an ion image for a specific mass/charge (m/z) ratio by increasing the detector gain (and thus sensitivity) for a particular time-of-flight arrival time. However, in these experiments, this is unable to fully suppress the significantly more intense signal corresponding to the intact precursor ion (CF_3CHO or CH_3CHO, 115 nm ionised). In the case of the CF_3^+ experiments, we found that the pulse energy of the VUV precursor light had to be increased slightly to account for a, likely, lower ionisation cross section leading to a greater precursor ion signal contaminating the centre of the image. Importantly, we note that this feature is present with the 308 nm pump laser shuttered. Furthermore, it is also known that photolysis of CH_3CHO clusters at 308 nm yields CO fragments that are rotationally cold and that varying molecular beam conditions from those that favour clusters to those where monomers are more abundant increases the population of higher CO rotational energy levels relative to lower ones [17]. Fig. S3 compares the CO photoproduct REMPI spectrum acquired from CF_3CHO under the molecular beam conditions used throughout this study (blue trace) with one recorded at half the seed gas concentration (red trace). This should significantly inhibit cluster formation if present. However, the distributions agree and there is no increase in the relative population of higher CO rotational energy levels allowing us to infer that the CO signal is arising dominantly from the photolysis of CF_3CHO monomers.

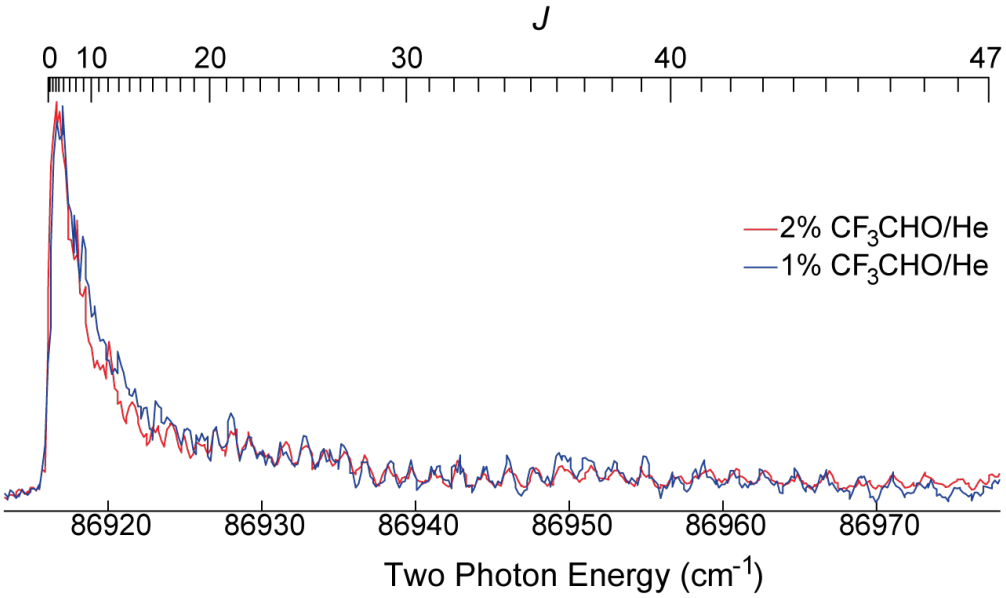

Figure S3: CO photoproduct REMPI spectra acquired following 308 nm photolysis of a jet-cooled sample of CF_3CHO at seed gas loadings of 2% (blue trace) and 1% (red trace).

Section S2 – Triple Fragmentation Channel R3

The predicted triple fragmentation pathway forming CF_2, HF and CO is a potential competing source of CO that warranted investigation. CF_2 and HF are difficult to probe using the ionisation methods above. HF does, however, have a very strong and well-understood infrared spectrum and, in contrast to CHF_3, is unlikely to be produced or consumed by secondary reactions of the radical photoproducts. This channel was thus investigated using Fourier-transform Infrared (FT-IR) spectroscopy with *in situ* photolysis. The experiment has been described in detail elsewhere [32]. Briefly, the photolysis laser used in the ion imaging experiment was directed (unfocused, ∼10 mm diameter) into a Teflon-coated, stainless-steel gas cell that was placed inside the evacuated chamber of a Bruker IFS 66 V/S FT-IR spectrometer. This cell was flushed and purged by means of a custom gas manifold that was then used to introduce the target gas. FT-IR spectra were then recorded before, during and after 308 nm laser irradiation. We irradiated 250 mTorr CF3CHO in 51.3 Torr helium bath gas for 10 minutes with the laser operating at 20 Hz with a pulse energy of ∼0.8 mJ. We anticipate that collisional quenching will be of minor importance at this low pressure of helium bath gas. The resultant FT-IR spectrum is presented, magnified about the HF region, as the red trace in Fig. S4 – revealing no evidence for HF.

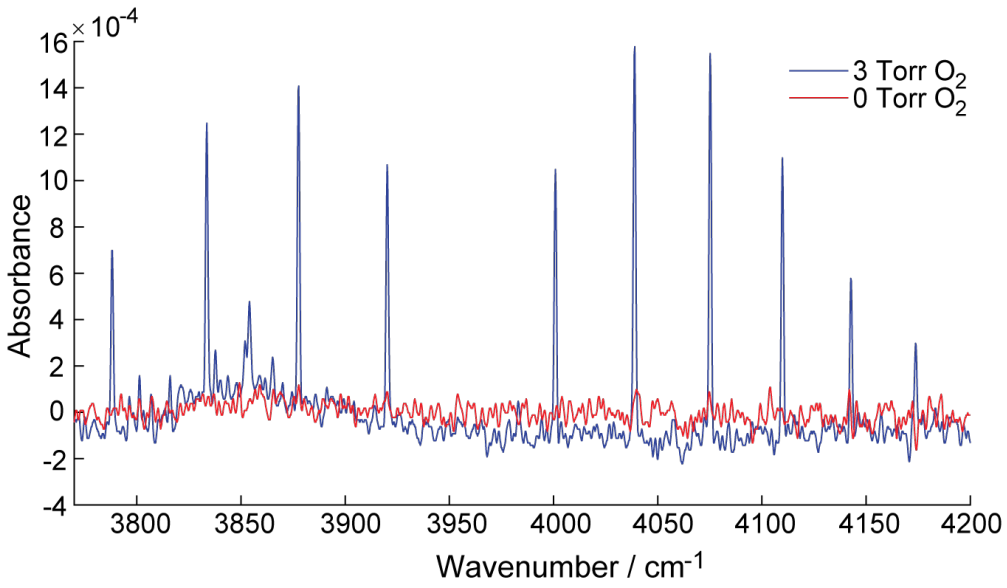

Figure S4: FT-IR spectra of the HF region following 308nm photolysis of a bulk sample of 0.5% CF_3CHO in helium (red trace) and with 3 torr O2 added (blue trace). The pronounced features in the blue trace that are absent in the read trace correspond to HF.

The second experiment was performed to measure the instrument sensitivity to HF. High quality FT-IR reference spectra are available for HF [34-36], but they needed to be scaled to the resolution and performance of the instrument used in this study. Preparing and using an authentic sample of HF gas presents safety, storage and transfer challenges. However, it is known that R1 in CF_3CHO ultimately leads to CO_2 and HF in the atmosphere by reaction of CF_3 with O_2 and then H_2O [6]. We thus added 3 Torr of O_2 to the sample, and repeated the experiment. This FT-IR spectrum is shown as the blue trace in Fig. S4 where features corresponding to HF are clearly visible. To determine the minimum detectable HF quantum yield we first performed a simple baseline correction by subtracting the mean signal intensity across the featureless region spanning 3940-3980 cm^{-1}. The intensity of the spectrum acquired with added O_2 was then linearly scaled down to a reasonable detection limit where the HF signal was just visible, but clearly identifiable, above the background provided by the spectrum acquired without additional O_2. These scaled data are shown in Fig. S5. Taking the root-mean-square-deviation of the red trace in Fig. S5 as the experiment noise leads to a signal/noise limit of 3.2 for the most intense HF feature. The area of this most prominent feature was then determined using trapezoidal integration and, by comparison to the equivalent feature in the reference spectrum [34-36], the minimum detectable concentration of HF was evaluated to be 2.1×10^{13} cm^{-3} for this specific experiment.

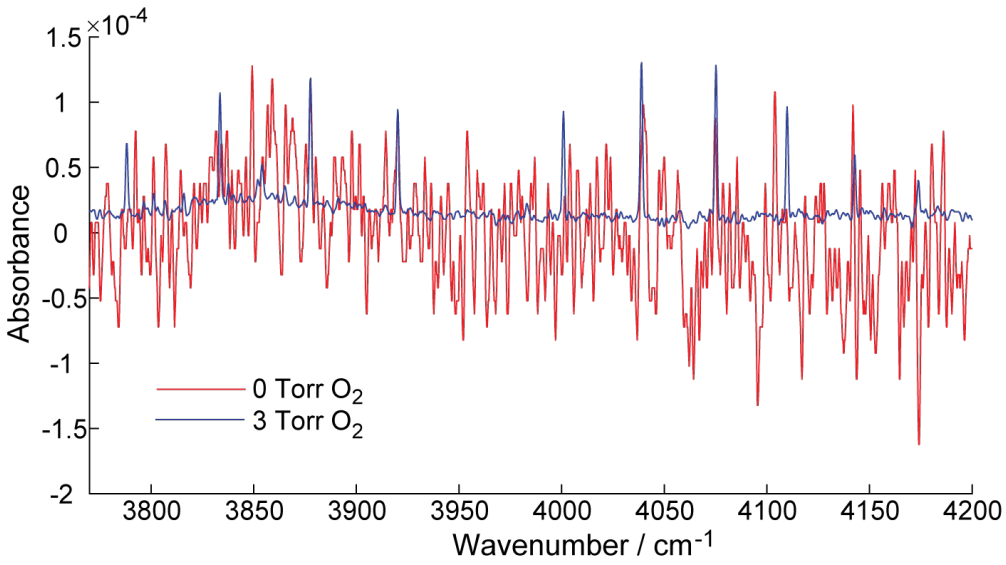

Figure S5: FT-IR spectra of the HF region following 308 nm photolysis of a bulk sample of CF_3CHO in helium (red trace), where HF is not present, and with 3 Torr of oxygen added (blue trace), where HF is present. The blue trace has been linearly scaled down to a reasonable HF detection limit against the red trace that is used as a proxy for the background.

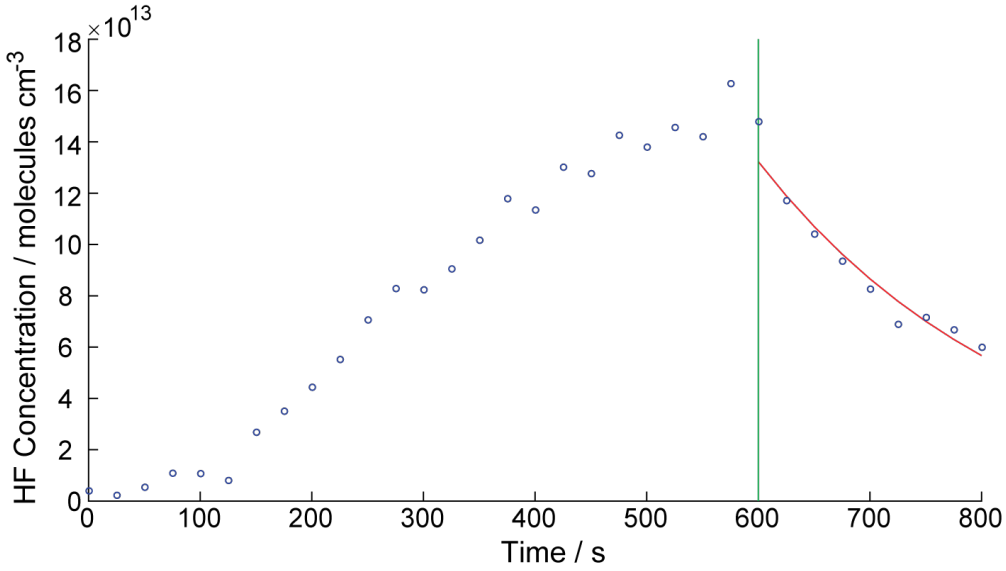

Figure S6: Time dependent concentration of HF determined by *in situ* FT-IR during 308 nm laser photolysis. The vertical green line at 600 s indicates the point at which the laser was turned off.

The loss of HF to the wall was observed over the course of these experiments and needed to be quantified to determine the minimum detectable quantum yield. Fig. S6 presents a time profile of the concentration of HF (determined as an average of the concentrations calculated using each HF feature) with each data point representing the conclusion of a 25 s measurement. The origin on the time axis corresponds to the photolysis laser being turned on and the vertical line indicates the photolysis laser being turned off. An exponential

decay was fitted to the laser-off component following photolysis and the first-order rate constant for HF loss to the cell wall was determined to be $k_{\text{wall}} = 4.2 \times 10^{-3}$ s^{-1}. The time dependance of HF concentration during the photolysis experiment is thus described by Equation (S1):

$$\frac{d[\text{HF}]}{dt} = k_{\text{photolysis}} - k_{\text{wall}}[\text{HF}] \tag{S1}$$

Where $k_{\text{photolysis}}$ is the pseudo-zeroth order rate constant describing the increase of [HF] from unimolecular photodissociation (*i.e.* hypothetical reaction pathway R3) and t is the photolysis time. Integration of Equation (S1) gives Equation (S2):

$$[\text{HF}] = (-e^{-tk_{\text{wall}}} + k_{\text{photolysis}})/k_{\text{wall}} \tag{S2}$$

Equation (S2) can be rearranged, making $k_{\text{photolysis}}$ the subject, to give Equation (S3):

$$k_{\text{photolysis}} = k_{\text{wall}}[\text{HF}] + e - tk_{\text{wall}} \tag{S3}$$

Substituting in $k_{\text{wall}} = 4.2 \times 10^{-3}$ s^{-1} determined above, as well as the detection limit of [HF] = 2.12×10^{13} cm^{-3} determined for $t = 600$ s, gives a minimum detectable $k_{\text{photolysis}} = 8.90 \times 10^{10}$ cm^{-3} s^{-1}. Ignoring wall loss, this results in a concentration of 5.34×10^{13} cm^{-3} at $t = 600$ s. This value of [HF], as well as the CF_3CHO absorption cross section at 308 nm [10], laser fluence and sample concentration, were used to determine a minimum detectable quantum yield for R3 of $\Phi(\text{R3}) = 0.07\%$. This value is substantially below the atmospheric pressure quantum yield that we determine for R2 (1.0%) and therefore definitely below that expected at the low pressure (250 mTorr) used in these experiments.

Section S3 – Quantum Yield calculations

As described in the main text, the relative quantum yield for CO from 308 nm photolysis of CF_3CHO and CH_3CHO, $\frac{\Phi_{\text{F}}}{\Phi_{\text{H}}}$, was determined according to Equation (S4):

$$\frac{\Phi_{\text{F}}}{\Phi_{\text{H}}} = \frac{\text{signal}_{\text{F}} \times \sigma_{\text{H}} \times J_{\text{H}}}{\text{signal}_{\text{H}} \times \sigma_{\text{F}} \times J_{\text{F}}} \tag{S4}$$

where signal_{F} and signal_{H} are the adjacent-baseline subtracted signal levels of CO ($J = 8$) for the two aldehydes, σ_{H} and σ_{F} the respective absorption cross sections at 308 nm [10], and J_{H} and J_{F} the $J = 8$ contribution to the full REMPI spectra. Survey REMPI spectra acquired over a short timescale immediately prior to the quantum yield measurements for each species are shown in Fig. S7. They are similar and, given the identical dynamics between the two species explained in the main text, as well as the rapid acquisition of the REMPI spectra, we assume that $\frac{J_{\text{H}}}{J_{\text{F}}} = 1$ *i.e.* that the REMPI spectra are identical for both molecules.

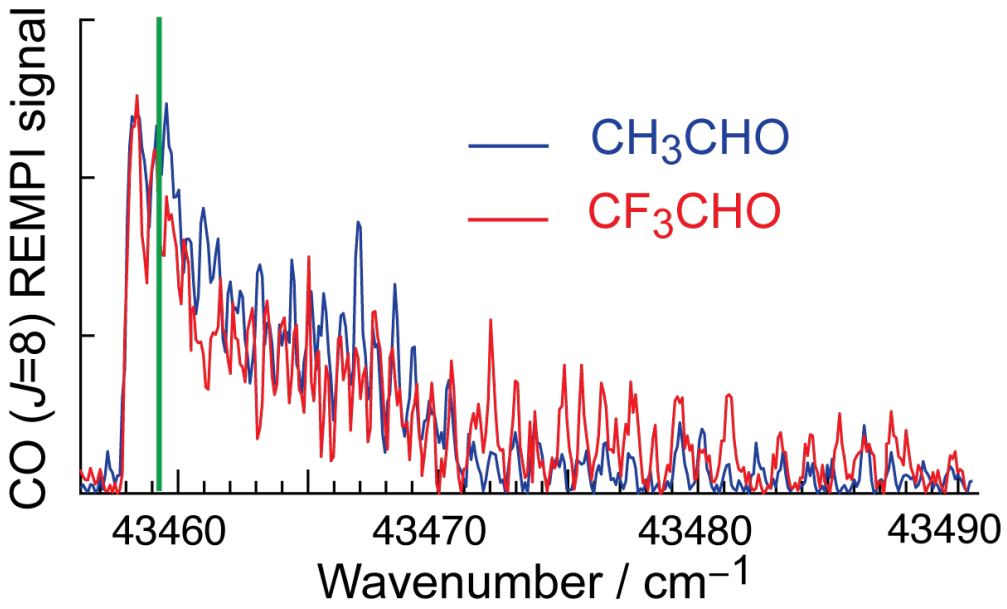

Figure S7: Survey CO photoproduct REMPI spectra acquired immediately before CO quantum yield determination for CF_3CHO and CH_3CHO with the photon energy corresponding to detection of CO($J = 8$) shown by a vertical green line.

Section S4 – Atmospheric Fate Calculations

The rate constant for photodissociation of CF_3CHO was calculated according to $k_{\mathrm{ph}} = \sum_{\lambda} j(\lambda)\sigma(\lambda)\Phi(\lambda)$ as described in the main text. For ease of reading, k_{ph} is the photolysis rate coefficient, $j(\lambda)$ the actinic flux, $\sigma(\lambda)$ the absorption cross section and $\Phi(\lambda)$ the photolysis quantum yield. We use the actinic flux for an overhead sun on a clear day from the US EPA [25] and the published absorption spectrum of CF3CHO [10]. The total photolysis quantum yield, Φ_{tot}, for CH_3CHO was calculated using the formula recommended by IUPAC [24] and based on the work of Moortgat and co-workers [14]. The quantum yield for R2, Φ_2, in CH_3CHO is taken from the fit in Fig. 4C of the main text. The R1 quantum yield, Φ_1, was calculated as the difference between Φ_{tot} and Φ_2. The total photolysis rate coefficient, k_{ph}(tot), was calculated from 290 to 340 nm, in 5 nm increments, using the CH_3CHO quantum yields (the fitted line in Fig. 4C) and 2.5× the CH_3CHO quantum yields as recommended in this work. The calculations were also performed for different OH mixing ratios corresponding to pristine and polluted conditions, as well as the measured global average [26]. Tables S1 and S2 show the actual values used in the calculations.

Table S1: Data used in the calculation of the photolysis rate coefficient.

Wavelength nm	j 10^{14} cm^{-2} s^{-1}	σ 10^{-20} cm^2	Φ_{tot}	Φ_1	Φ_2	$j\sigma\Phi_1$ 10^{-7} s^{-1}	$j\sigma\Phi_2$ 10^{-8} s^{-1}
290-295	0.001	2.7	0.592	0.570	0.022	0.02	0.006
295-300	0.041	2.9	0.517	0.504	0.013	0.59	0.157
300-305	0.398	2.9	0.418	0.407	0.011	4.65	1.253
305-310	1.41	2.7	0.298	0.288	0.010	11.03	3.940
310-315	3.14	2.0	0.181	0.171	0.010	13.63	8.037
315-320	4.35	2.2	0.094	0.084	0.010	8.15	9.678
320-325	5.48	1.9	0.044	0.034	0.010	3.54	10.36
325-330	7.89	1.5	0.019	0.009	0.010	1.09	11.60
330-335	8.35	1.1	0.008	0.000	0.010	0.00	9.185
335-340	8.24	0.74	0.004	0.000	0.010	0.00	6.098

$$k_{ph}(\text{R1}) = 4.27 \times 10^{-6} \text{ s}^{-1}$$
$$k_{ph}(\text{R}) = 6.4 \times 10^{-7} \text{ s}^{-1}$$
$$k_{ph}(\text{tot}) = 4.91 \times 10^{-6} \text{ s}^{-1}$$

Table S2: Atmospheric fate of CF_3CHO, using 2.5× CH_3CHO quantum yield for R2

[OH] 10^6 cm^{-2}	k'(OH) 10^{-7} s^{-1}	k_{ph} 10^{-6} s^{-1}	k_{tot} 10^{-6} s^{-1}	Half life hours[a]	%OH reaction	%R1	%R2 (% HFC)
0.50	2.40	4.91	5.15	37	5%	83%	12%
1.1	5.28	4.91	5.44	35	10%	79%	11%
5	24	4.91	7.31	26	33%	58%	9%

[a] under constant irradiation

Supplementary References

[34] T. J. Johnson, L. T. M. Profeta, R. L. Sams, D. W. T. Griffith, and R. L. Yokelson. An infrared spectral database for detection of gases emitted by biomass burning. *Vibrational Spectroscopy*, 53(1, SI):97–102,2010.

[35] S. W. Sharpe, R. L. Sams, T. J. Johnson, P. M. Chu, G. C. Rhoderick, and F. R. Guenther. Creationof 0.10 cm^1 resolution quantitative infrared spectral libraries for gas samples. In S. D. Christesen andA. J. Sedlacek III, editors, Vibrational Spectroscopy-based Sensor Systems, volume 4577, pages 12 – 24. International Society for Optics and Photonics, SPIE, 2002.

[36] S. W. Sharpe, T. J. Johnson, R. L. Sams, P. M. Chu, G. C. Rhoderick, and P. A. Johnson. Gas-phase databases for quantitative infrared spectroscopy. *Applied Spectroscopy*, 58(12):1452–1461, 2004